Magnetic Compensation Loop Design using Transient ESTER/PHOENICS MHD Simulations

Amit Jha
Senior Scientist
Aditya Birla Science and Technology Company (P) Ltd, Navi Mumbai, Maharashtra, India
Corresponding author: amit.jha@adityabirla.com

Abstract

Magnetohydrodynamic (MHD) instability or waves at the metal-bath interface in the aluminium reduction cell is the major hurdle for increasing energy efficiency and productivity. The vertical magnetic field and horizontal currents in the metal interact to produce the Lorentz force which is mainly responsible for the growth of the interfacial waves. To stabilize the interface at a smaller anode-cathode distance and higher anode current density, a magnetic compensation loop has been designed without altering the existing busbar system. The effect of magnetic field compensation loops inside, outside, and on both sides of the potline circuit has been evaluated. The bath-metal interface was studied using ESTER/PHOENICS, built specifically for MHD simulations of aluminium reduction cells. Transient simulation of the interface waves was used to study the effect of vertical magnetic field bias from a neighboring potroom. Interface position was tracked with time after introducing the initial perturbation. It was observed that the magnetic compensation loop installed on both sides (tap and duct side) of the potrooms gives the most stable interface.

Keywords: Aluminium reduction cells, Magnetohydrodynamic instability of reduction cells, Magnetic compensation, Horizontal current, Vertical magnetic field, ESTER/PHOENICS.

1. Introduction

Aluminium is produced by electrolysis of alumina dissolved in a cryolite bath at a typical temperature of 950 – 970 °C in a Hall-Héroult cell. Liquid aluminium produced from the reduction process gets deposited on the cathode surface. A liquid-liquid interface exists between the bath on top and aluminium at the bottom. Aluminium and bath are in continuous motion, primarily driven by the electromagnetic Lorentz force. The Lorentz force is generated by the interaction between the electric current passing through the liquids and the magnetic field generated due to the current carrying components in and around the cell. The CO_2 gas is generated as the byproduct of the electrolysis below the anode and also drives the bath. The electric current enters the cell through anodes, passes through the liquid bath, aluminium, carbon cathode, and exits via cathode collector bars. Busbars connected to the cathode collector bars carry the electric current to the next cell. A potline in an aluminium smelter has two potrooms and each potroom has many cells connected in series. The electric current from the rectifier enters through one potroom of the potline and exits from another, forming a closed loop. Aluminium smelters across the world are known to operate at amperages between 60-660 kA, with a cell voltage of 3.5-4.5 V, depending on the design [1]. The specific energy required to produce aluminium can be as high as 14 DC kWh/kg Al [2], or even greater in some smelters. Out of the total energy consumption, 40 – 50 % is required for the electrolysis and the rest is dissipated as heat. The electrical resistance offered by the layer of bath between the interfaces of anode-bath and aluminium-bath is the highest [2] and contributes most to the heat generation in the cells. This layer is known as anode-cathode distance (ACD) and may vary between 25 to 45 mm across different smelters.

To improve overall energy efficiency, a very thin layer of ACD is required. Amperage increase in the potroom is also followed by a reduction in ACD to avoid any major change in internal heat generation. The MHD instability at the aluminium-bath interface is the major obstacle and limits the minimum value of ACD. The MHD instability or waves at the interface may grow upon lowering of ACD, resulting in frequent contacts between the aluminium-bath interface and the anode, thus, allowing the electric current to pass without electrolysis. This loss of current efficiency increases the specific energy required to produce aluminium. Therefore, an aluminium smelter needs upgrades to have better MHD stability which will support productivity increase as well as reduction of specific energy consumption.

MHD instability has been understood as a large wavelength (> 1 m) disturbance [3, 4] of rotating nature [5], which can more clearly be expressed as coupled longitudinal and transverse modes of the wave [6, 7]. Redistributed horizontal current due to the longitudinal mode will interact with the vertical magnetic field to produce a force that excites the transverse mode and vice-versa. The resonating modes interact and feed energy to each other to grow the wave amplitude. Potocnik [6] used a 3D MHD transient model on ESTER to study the interaction of the longitudinal and transverse waves of different harmonics and found a strong relation between (1,0) and (0,1) modes. A bias in the vertical magnetic field, i.e., the non-zero average value over the liquid metal area, due to the effect of neighboring potroom(s) leads to a Lorentz force distribution which is detrimental to interfacial instability [8, 9, 10]. Urata [4] and Potocnik [6], both reported a strong dependence of interfacial stability on vertical magnetic field distribution. Antisymmetric distribution of the vertical magnetic field in the liquids has been recommended for better stability [11].

The interaction of the longitudinal and transverse modes for a uniform vertical magnetic field (B_z) is shown in Figure 1, as explained by Urata [7]. Figure 2 sufficiently illustrates the interaction of waves for an antisymmetric distribution of the vertical magnetic field. The directions of the vertical magnetic field, the horizontal current of the perturbed interface ($j_{i=1,2,3}$), and the perturbed Lorentz force component ($f_{i=1,2,3}$) at the interface are shown in the illustrations.

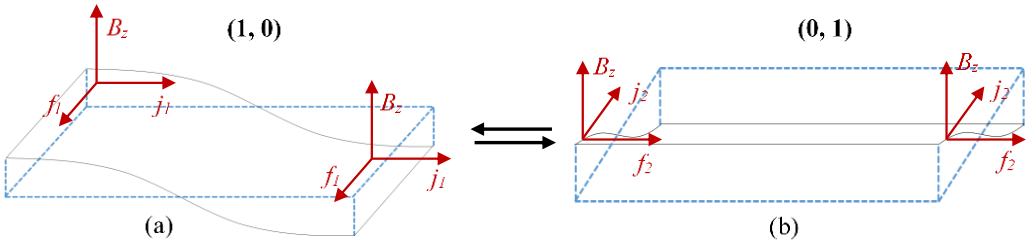

Figure 1. (a) Lorentz force (f_1) along cell width generated due to j_1 and uniform B_z, which leads to the generation of (0, 1) mode, (b) f_2 along cell length generated due to j_2 and uniform B_z, exciting (1, 0) mode.

Figures 1(a) and (b) show (1, 0) and (0, 1) modes at the interface, respectively. In Figure 1(a), the current density increases in the bath layer at the location where the interface comes closer to the anode bottom, resulting in a horizontal current (j_1) in liquid aluminium directed away from the wave crest. The uniform B_z interacts with the horizontal current to produce a component of Lorentz force (f_1) along cell width, due to which the interface gets tilted, resulting in the (0, 1) mode shown in Figure 1(b). The (0, 1) mode at interface generates horizontal current (j_2) along

cell width, which interacts with B_z to produce a Lorentz force component along cell length. The Lorentz force (f_2) adds to the momentum of the interface moving down, resulting in increased wave amplitude. The forces along cell width and length as a result of (1, 0) and (0, 1) mode respectively, keep driving (0, 1) and (1, 0) mode. The mechanism is now applied to the case of an anti-symmetrically distributed vertical magnetic field in Figure 2. The directions of the vertical magnetic field, the horizontal current, and the resultant force in the four quadrants of the cell are shown in Figure 2. The antisymmetric magnetic field distribution results in a slightly complicated force distribution with the initial (1, 0) mode at the interface. The force will lead to generation of the (0, 2) mode at interface, with opposite orientations at the two ends, as shown in Figure 2(b). The magnitude of the horizontal current (j_3) along cell length in Figure 2(b) will be smaller than that of the (0, 1) mode in Figure 1(b). Hence, the destabilizing force (f_3) along cell length in Figure 2(b) will also be smaller. Thus, the lower modes at the interface break into higher modes resulting in relatively smaller instability in the case of an antisymmetric vertical magnetic field. Therefore, to enhance MHD stability, the bias of the vertical magnetic field due to neighboring potroom(s) or busbars must be compensated to achieve the magnetic field distribution favoring stability.

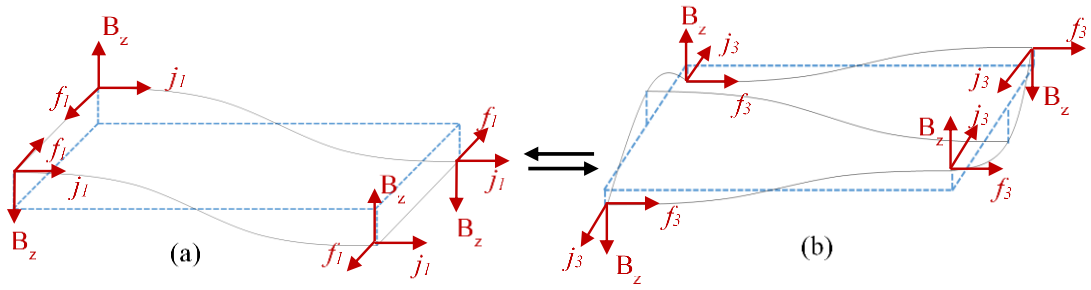

Figure 2. The illustration shows the interaction of waves for an antisymmetric B_z, (a) Lorentz force in the case of (1, 0) mode for antisymmetric B_z, and (b) modes at interface generated as a result of (a).

Design principles for the busbar system with desired magnetic field distributions are reported earlier [11]. The magnetic field can be compensated internally by modification of the busbar system as well as externally by placing a current-carrying magnetic compensation loop near the potline. A magnetic compensation loop (MCL) can be a practical solution for most of the operating potlines, with only a few exceptions, as the space constraints can be a challenge for the older potlines. Retrofitting can be a costly affair and will be a trade-off between energy saving, productivity, and investment for new busbars, civil works, and installation. In this paper, the working and design principles of the MCL are discussed for a potline at 420 kA. ESTER/PHOENICS is used to perform MHD transient simulations of the aluminium-bath interface. The effect of the initial perturbation on the aluminium-bath interface is studied for three different designs of the MCL. The best configuration of MCL is identified by comparing the amplitudes of the interfacial wave.

2. Working of the MCL

The electric current passing through A-room of a potline schematic shown in Figure 3 produces the negative B_z in B-room cells and vice-versa as shown in Figures 4(a) and (b). The working of MCLs to compensate for the negative B_z is illustrated in Figures 4(c), (d), and (e), for the given potline configuration.

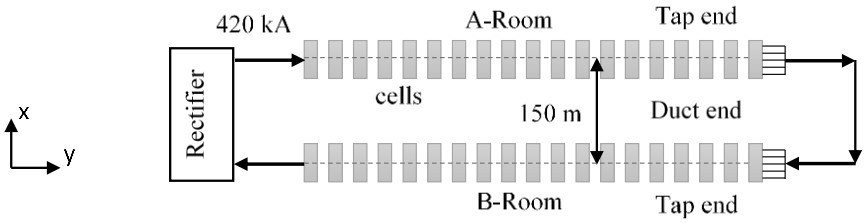

Figure 3. Potline schematic with clockwise current, top view.

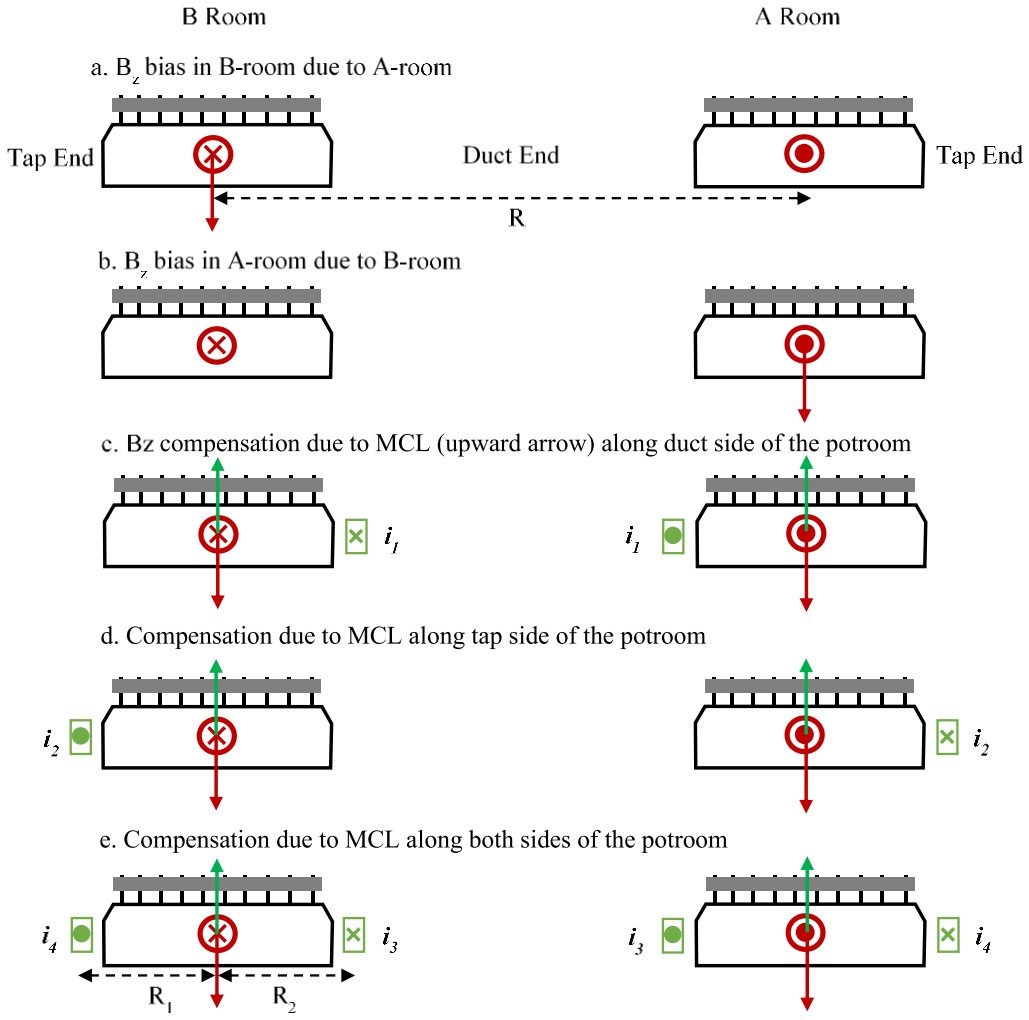

Figure 4. The B_z bias due to the neighboring potroom and working principle of MCL.

The negative bias of B_z in each room is shown by the downward arrows in Figure 4. ⊗ and ⊙ refers to the direction of the electric current in and out of the plane, respectively. To compensate for the B_z bias, current carrying conductors can be placed either along the duct side, or the tap side, or on both sides of the potroom, as shown in Figures 4(c), (d), and (e), respectively. The busbar along the duct end should carry electric current in the same direction as it is in the potroom, whereas, the direction of electric current should be opposite to the potline current in the busbar placed along the tap end. The magnitude of the B_z bias in mT at the center of the cell can be approximately calculated as $I/(5R)$, where, I is the potline current (kA) and R is the distance (m)

between the centrelines of the two rooms. In the case of the duct-end or tap-end MCL only, the MCL current, which fully compensates B_z bias at the cell centre, will be, $I_L = {}^{I}/_{R} \times R_L$, where R_L is the distance between the MCL busbar and the center of the cell. The B_z bias can be made zero at the cell center, but it will get overcompensated near the cell end adjacent to the loop. To reduce the overcompensation of B_z, the MCL at both ends, i.e., duct and tap end of the cell, carrying a smaller current than the single-sided MCL but enough to provide the required compensation, should be the best option. The electric current in busbar at both ends will be the same if the whole MCL system is powered by the same rectifier. The magnetic field produced by the busbar on each side can be adjusted by choosing the appropriate distance between the cell center and the busbars. In case, the duct end loop and tap end loop are powered independently by different rectifiers, then the electric current can be tuned depending on the space available in the potroom to install the busbar.

ESTER requires magnetic field as input, either in a file or as second order polynomial for B_x, B_y, and B_z. The polynomials are already programmed in ESTER, and the user has to specify polynomial coefficients only [12]. For the basecase discussed in the paper, the magnetic field distribution along length of the cell is shown in Figure 5. The analytical relations (1, 2, and 3) were used to generate the field (B_x, B_y, B_z) along x, y, and z directions in the cell.

$$B_x = -7.784 - 0.014x + 9.121y + 0.166x^2 - 0.047x^2y \quad (1)$$

$$B_y = -0.058 - 0.302x + 0.091y + 0.032xy + 0.001y^2 - 0.001xy^2 \quad (2)$$

$$B_z = -0.549 + 0.077x - 0.015y + 0.070xy \quad (3)$$

The legends, y = 2.1, 0, and -2.1 corresponds to the distance (m) of an imaginary line in the metal along the cell length at downstream anode edge, center, and upstream anode edge, respectively. The circled portion in the plot shows that the B_z bias in this case is greater than 0.5 mT at the cell centre.

Now considering the cases – 1, 2, and 3 of MCL design; (a) duct end (DEMCL), (b) tap end (TEMCL), and (c) both sides (DETEMCL) loop, respectively. The amount of current through the MCL, and the distance between the MCL and cell center are shown in Table 1.

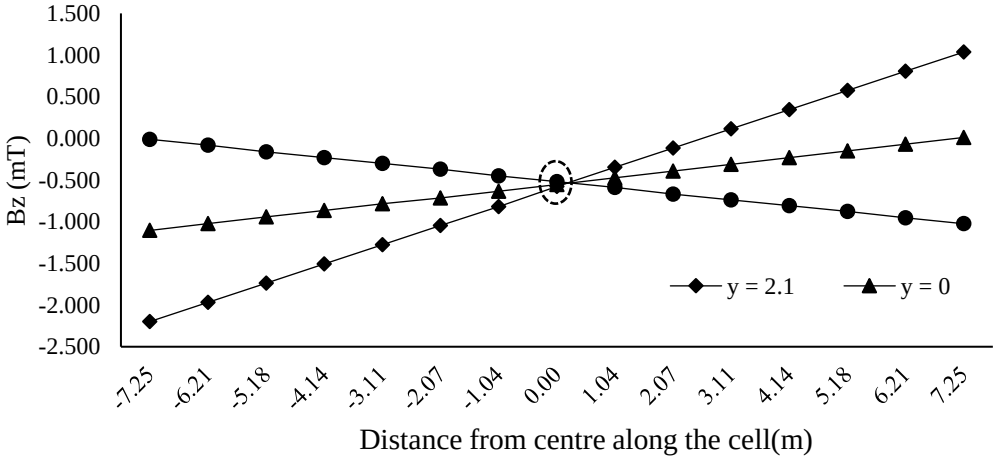

Figure 5. B_z distribution along cell length.

Table 1. Description of MCL cases considered for analysis.

		MCL current (kA)	Distance from cell centre (m)	B_z (mT) at centre due to MCL
DEMCL	Case – 1	30	10.75	0.56
TEMCL	Case – 2	30	10.75	
DETEMCL	Case – 3	15 + 15 (tap + duct end)	10.75	

The B_z variations along the centerline of the cell are shown in Figure 6 for all cases. The B_z due to the compensation loops were superimposed with that of the basecase to obtain the final distribution of the magnetic field. The B_z is compensated at centre of the cell for all three cases of MCL, but a non-uniformity can be observed at the ends, which is of course least for case – 3.

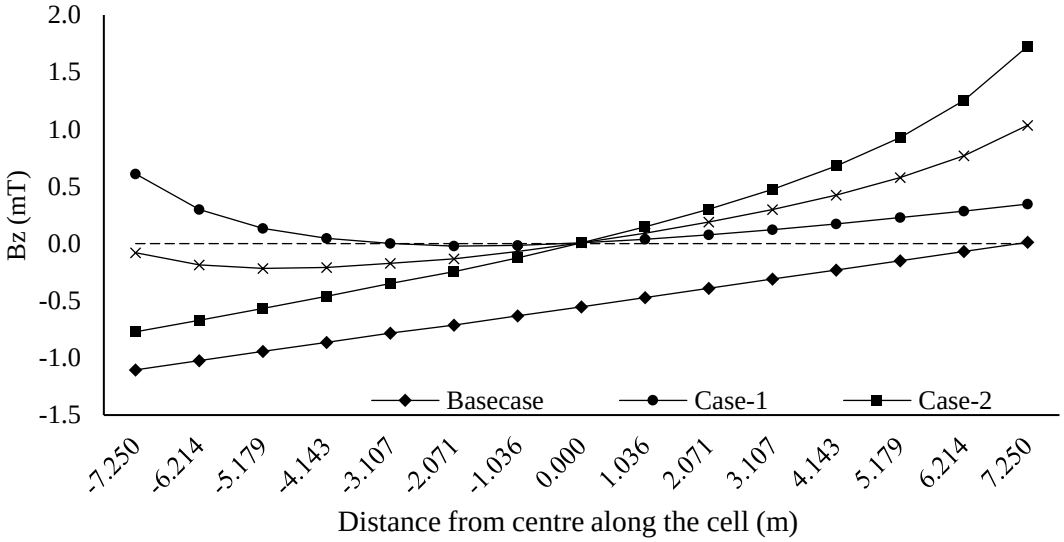

Figure 6. Bz variation due to MCL.

3. MHD Modelling

The software package ESTER/PHOENICS was used for the computational analysis. ESTER is the special purpose program developed in PHOENICS to predict flow profile and bath-metal interface deformation under steady state and transient conditions [12]. The 3D model of the aluminium reduction cell was created for the domains shown in Figure 7. To reduce computation time, initial simulations were performed using the domain shown in Figure 7(a). The best configuration of MCL was identified based on the initial results, and the same was further analyzed in detail, based on the domain shown in Figure 7(b).

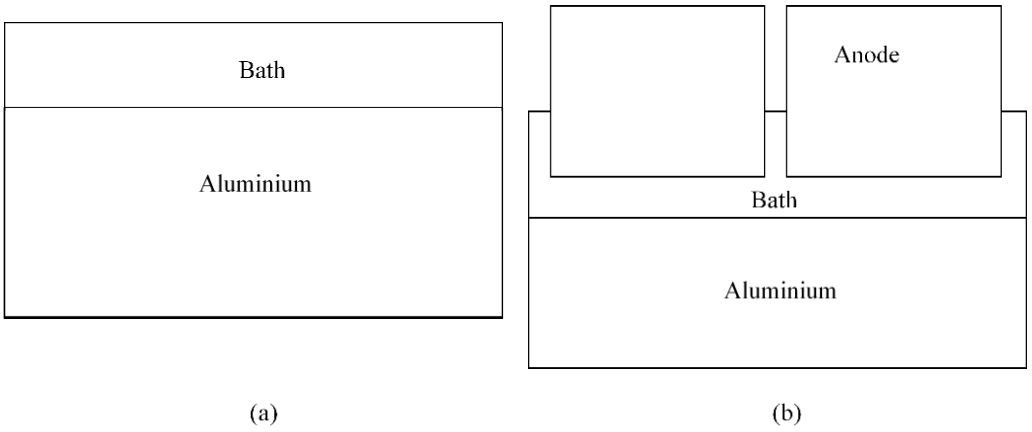

Figure 7. Model geometry of trial setup for MHD calculations.

The effect of gas bubbles movement on hydrodynamics of aluminium and bath is ignored. Ester calculates the imposed electric current distribution using generalized Ohm's law (4).

$$\mathbf{J} = \sigma(\mathbf{E} + \mathbf{v} \times \mathbf{B}) \tag{4}$$

where:

J	Current density vector, A/m^2
σ	Electrical conductivity, S/m
E	Electric field vector, V/m
u	Velocity, m/s
B	Magnetic induction, T and
x	Vector cross product.

The second term of equation (4) is flow-induced electric current in magnetic field. This term is incorporated in ESTER as a toggle switch and can be turned on or off by the user. In this study, it was set off. As electrical boundary conditions, voltage at the top of the bath in domain (a) and at the top of the anode in domain (b) is fixed, and a realistic vertical current distribution given by (5), also shown in Figure 8, is applied at the bottom of the aluminium layer. The current distribution at interface is obtained using electromagnetic boundary conditions at the interface: continuity of the normal component of current density, and the tangential component of electric field. These are already incorporated in ESTER [12].

$$J_z = -1260.17y^2 - 5000 \tag{5}$$

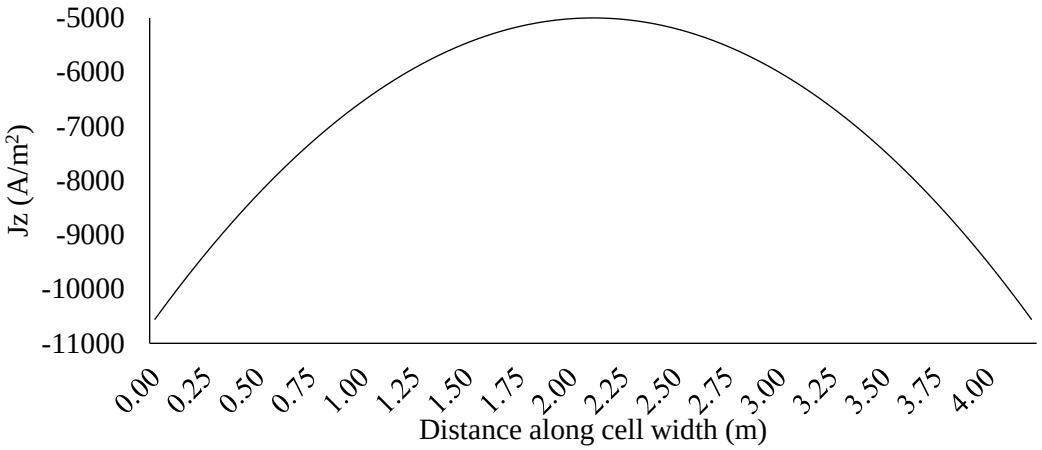

Figure 8. J_z on cathode surface.

The magnetic field required for MHD calculations is generated using analytical expressions in ESTER., and was discussed earlier. Conservation of mass (6), and momentum equations (7), with Lorentz force (8) as the source term are used to obtain the pressure distribution and flow. The conditions of no-slip and free-slip are applied near the walls and free boundaries, respectively. The simulations were performed considering turbulent flow with a constant viscosity model, but with very low turbulent viscosity coefficient, amounting to using laminar viscosity, to obtain slow damping of the waves. ESTER uses the floating grid principle to track the interface of aluminium and bath [12].

$$\nabla \cdot \boldsymbol{u} = \mathbf{0} \tag{6}$$

$$\rho \frac{\partial \boldsymbol{u}}{\partial t} + \rho(\boldsymbol{u} \cdot \nabla \boldsymbol{u}) = -\nabla p + \mu \nabla^2 \boldsymbol{u} + \boldsymbol{F} \tag{7}$$

$$\mathbf{F} = \mathbf{J} \times \mathbf{B} \tag{8}$$

where:

u	Velocity vector, m/s
t	Time, s
ρ	Density, kg/m^3
p	Pressure, Pa
μ	Dynamic viscosity, Pas and
F	Lorentz force, N/m^3

Dimensional analysis of electromagnetic equations shows that the magnetic Reynolds number (9) is smaller than 0.2, hence, the magnetic field is not influenced by the metal flow. So, this effect can be ignored.

$$R_m = vL\mu_{Al}\sigma \tag{9}$$

R_m	Magnetic Reynolds number
v	Characteristic velocity, m/s
μ_{Al}	Magnetic permeability of liquid aluminium, (Tm)/A
σ	Electrical conductivity, S/m

Table 2 shows model description and relevant mesh information.

Table 2. MHD model description.

Geometric and operating parameters		
Operating line current, (kA)	420	
Metal height, (m)	0.18	
Bath height, (m)	0.18	
ACD, (m)	0.05	
Anode height at mid-life, (m)	0.29	
Length of the cell, (m)	14.5	
Width of the cell, (m)	4.2	
No. of anodes	20	
Gap between anodes along cell length and width, (m)	0.050, 0.200	
Gap between anode and sidewall along cell length and width, (m)	0.100	
Relevant mesh Information	Domain	
	(a)	(b)
No. of cells along each anode length	-	5
No. of cells along each anode width	-	3
No. of cells in inter anode gaps	-	2
No. of slabs in anode (along ***z*** direction)	-	4
No. of cells between anode and sidewall	-	2
No. of cells in aluminium along cell length	20	
No. of cells in aluminium along cell width	6	
No. of slabs in Aluminium (along ***z*** direction)	6	6
No. of slabs in bath (along ***z*** direction)	4	4

4. Results and Discussion

The simulations were performed for 1500 seconds at the time steps of 0.20 second after introducing initial perturbations. First, to check the accuracy of results, the oscillation period from the analytical relation of internal gravity waves is compared with that of the ESTER simulation, for a primary perturbation of the (1, 0) mode with an amplitude of 0.02 m. Subsequently, the illustration presented in Figure 2 was also investigated using simulations to observe breaking of the (1, 0) mode into the higher modes in presence of the antisymmetric B_z. The interfaces of the basecase, case-1, 2, and 3 were analyzed after an initial perturbation of ± 0.020 m (at ends) along the cell length as shown in Figure 9.

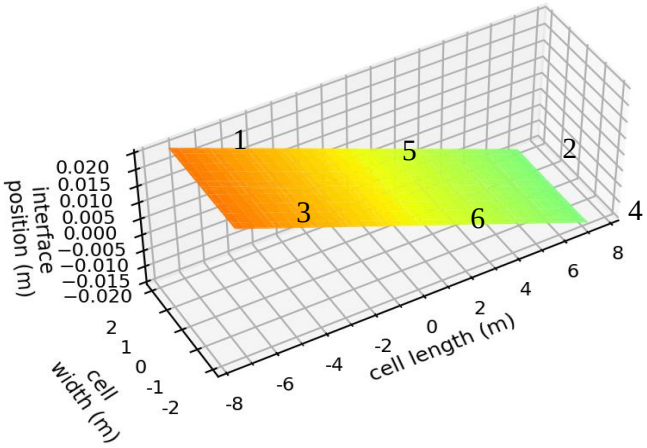

Figure 9. Initial interface perturbation.

5. Internal Gravity Waves

The oscillation of the interface with time for (1, 0) mode with and without channels between the anodes, is plotted in the Figure 10. For ACD = 20 cm, the oscillation period without the channels comes out to be 140 seconds, which is close to the value of 152 seconds obtained using the analytical relation [6, 13]. A realistic anode geometry with channels in between, results in the oscillation period of ~200 seconds.

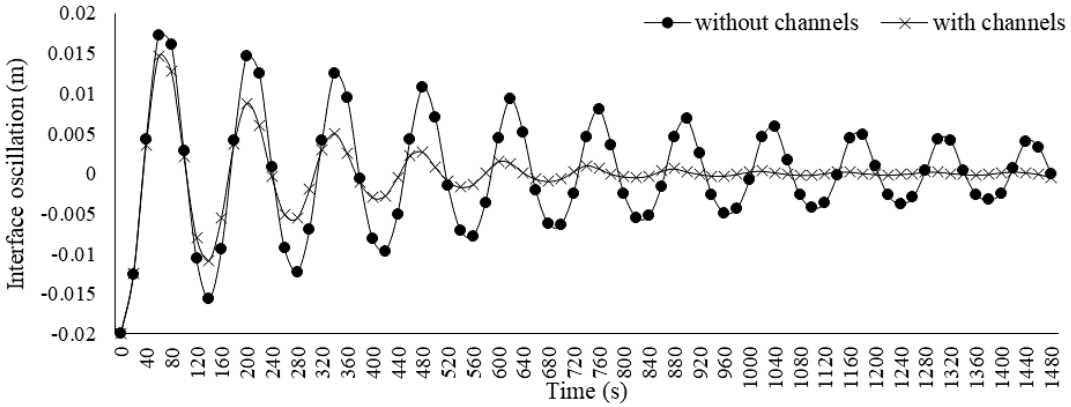

Figure 10. Interface oscillation under the effect of gravity, with anode.

6. Investigation of Interfacial Waves with Antisymmetric B_z

An antisymmetric B_z results in force distribution which breaks large wavelength waves into smaller ones as shown in Figure 2. The smaller wavelength results in destabilizing force of smaller magnitudes, which keeps decreasing after every cycle. The MHD simulation was performed for a perfectly antisymmetric B_z. The interface with initial perturbation as shown in Figure 9 shows formation of higher modes with smaller wavelengths as shown in Figure 11. The (0, 2) modes can clearly be seen near both short ends, which are out of phase with each other. One can also notice that the interface is almost flat in specific regions at the highest position and (0, 2) mode can be seen as a 'hump', at a gap from the end. The reason for this, is very much smaller horizontal current under perturbed condition just near the highest position of the interface.

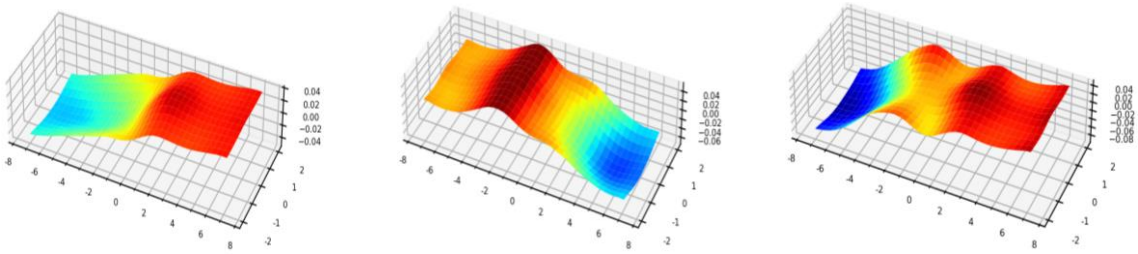

t =76 s t =160 s t =240 s

Figure 11. Interface obtained from MHD simulation for the illustration in Figure 2.

7. Analysis of Interface with Basecase B_z

Initially, quick simulations were performed considering layers of liquid aluminium and bath only, as shown in Figure 7(a). The oscillations of interfacial point at the corner (1, 2, 3, and 4) and at center (5 and 6) for the basecase are plotted with time as shown in the Figure 12. It can be observed that:

- Difference between maxima and minima of interface during any cycle is approximately 0.03 m for the points 1 and 2. The points 3, and 4 have maximum deviation of 0.05 m.
- Corner points 1 and 3 were completely out of phase with the points 2 and 4, respectively, which indicated the presence of (1, 0) mode (see Figure 12(a), and (b)).
- Point 5 was found to be out of phase with both the corner points 1 and 2, as well as the point 6 was also showing similar behavior with respect to the points 3 and 4, indicating the presence of other higher modes (see Figure 12(c), (d), (e), and (f)).
- None of the interfacial points were showing the stabilizing trend.

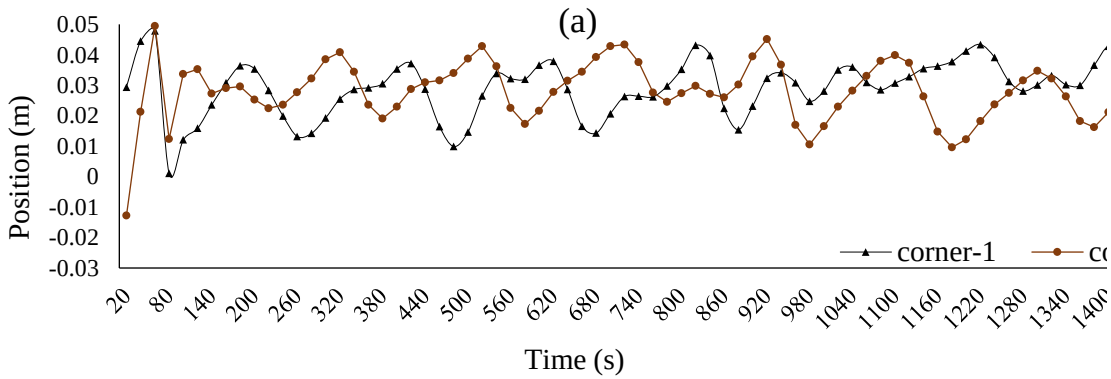

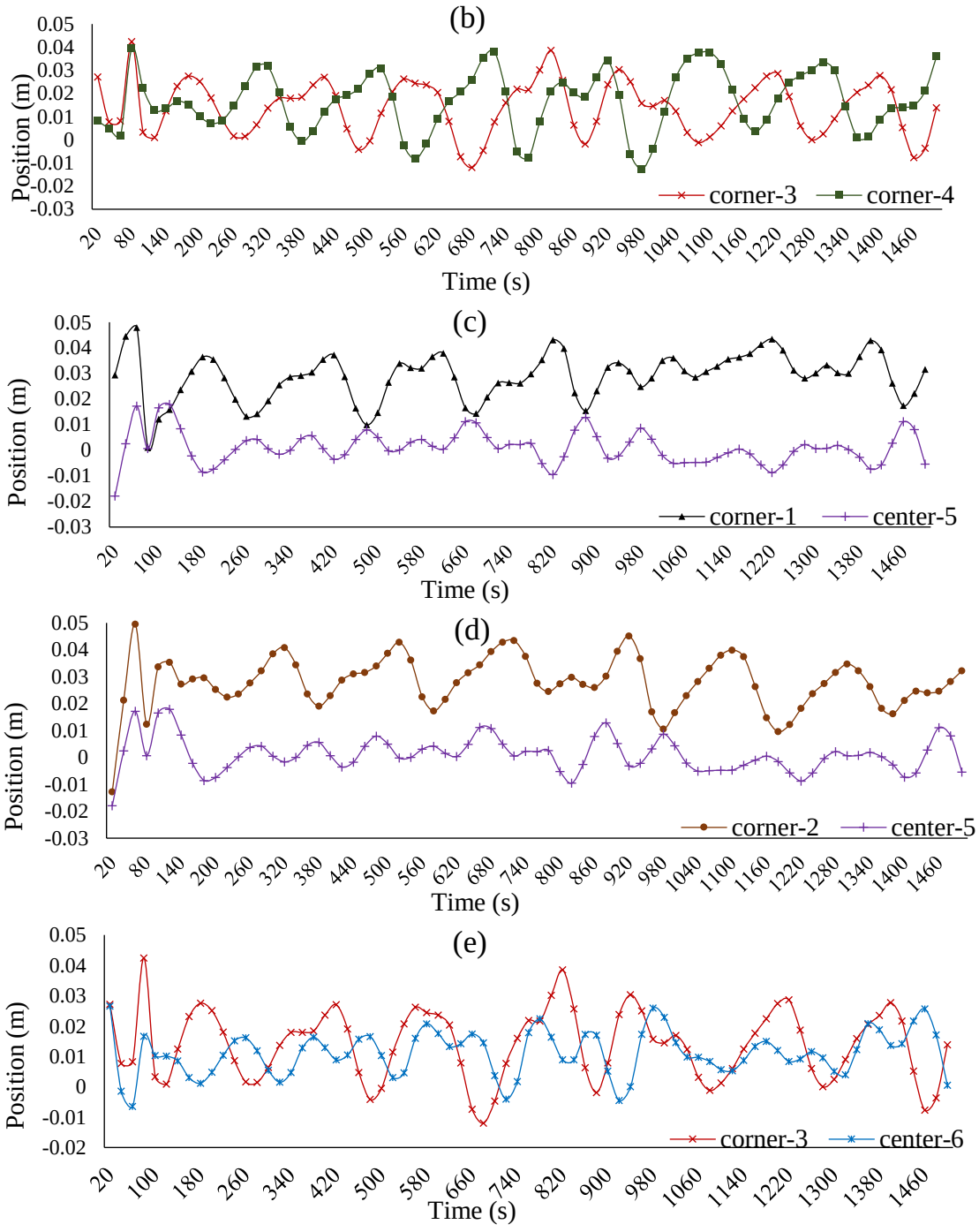
(b)
Position (m)
Time (s)
corner-3
corner-4
(c)
Position (m)
Time (s)
corner-1
center-5
(d)
Position (m)
Time (s)
corner-2
center-5
(e)
Position (m)
Time (s)
corner-3
center-6

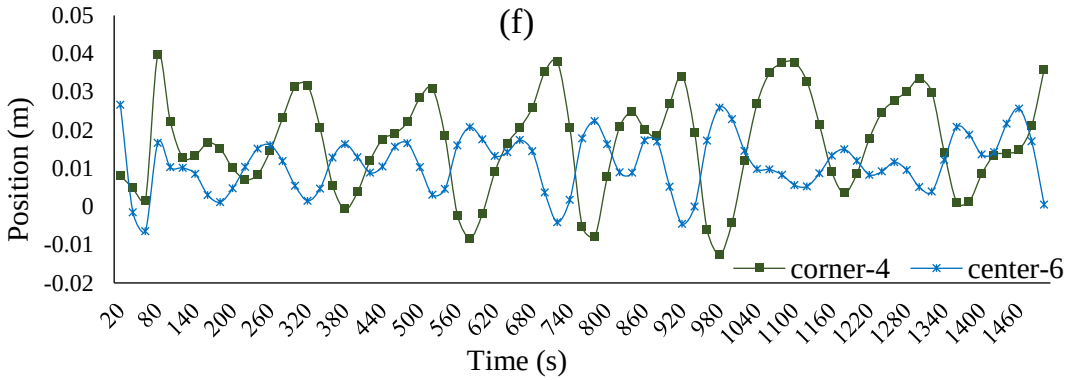

Figure 12. Position of interface points for basecase.

8. Comparison of Cases-1, 2, and 3 of MCL

The oscillation of the interface corners is plotted in Figure 13 for the cases of MCL described in Table 1. The interface oscillation can be observed to be on the reducing trend for case-1 to 3, and faster for the case-3, implying it (MCL on both sides of the cell) to be the most stable configuration. Therefore, further detailed analysis was performed for the basecase and case-3, using the domain shown in Figure 7(b) (including the anode assembly).

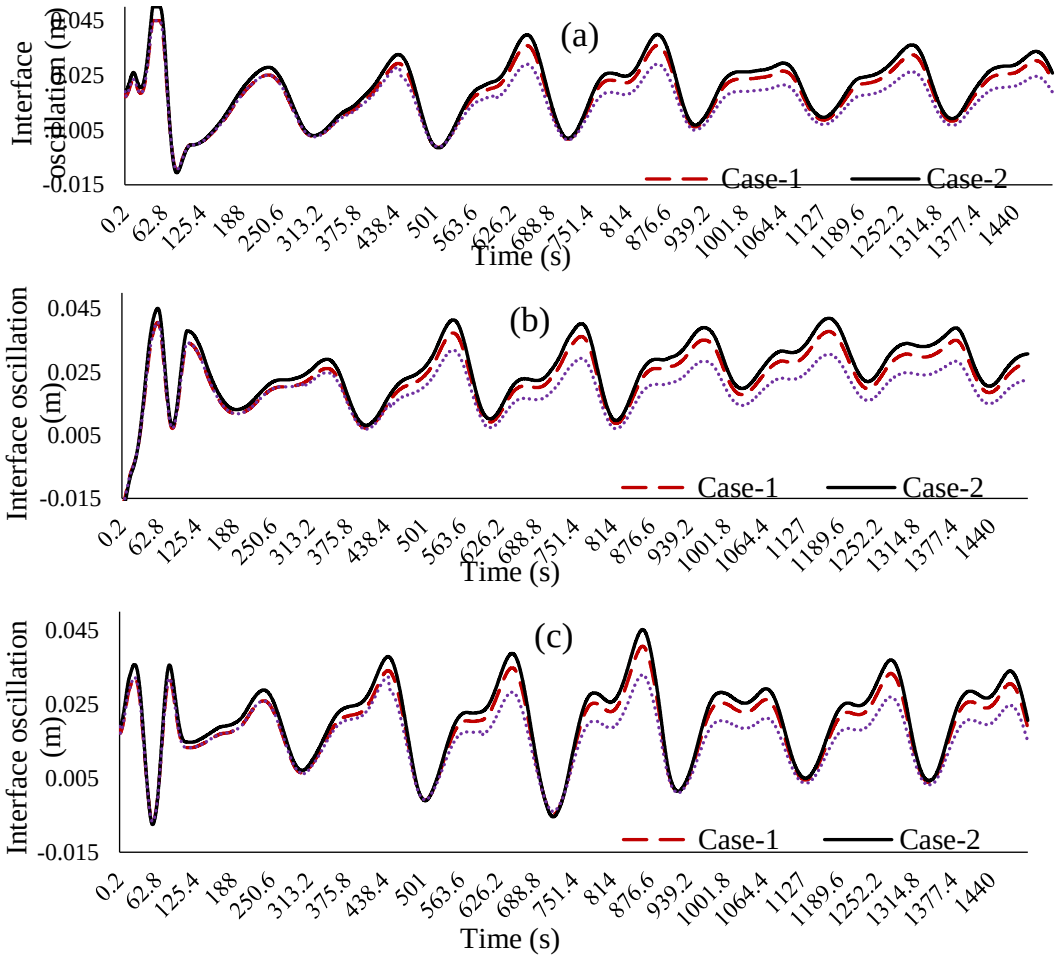

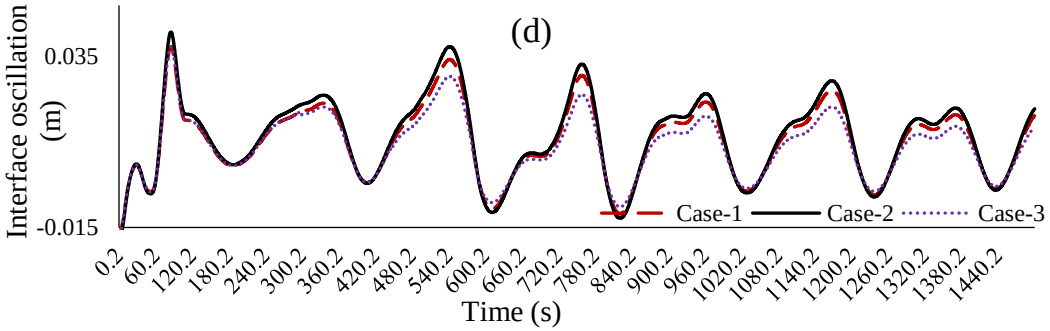

Figure 13. Position of interface corners (relative to Z=0.18 m), (a) corner – 1, (b) corner – 2, (c) corner – 3, and (d) corner – 4.

9. Detailed Analysis and Comparison of the Basecase and Case-3

The position of interfacial points was obtained from the MHD simulations, and used to calculate the amplitude of the dominant spatial frequency using Fourier transform. The maxima of amplitudes were calculated for 5 different lines along cell length on the interface. The amplitudes (average of the maximum values corresponding to the 5 lines on the interface) of the interfacial wave with time are compared for the basecase and case-3 in Figure 14. It can be observed that, the amplitudes of the case-3 interface are smaller than that of the basecase for most of the time, which indicates better stability of case-3. It can also be observed that the amplitude of case-3 interface waves is on a reducing trend after 920 seconds, whereas, it continues to grow for the basecase.

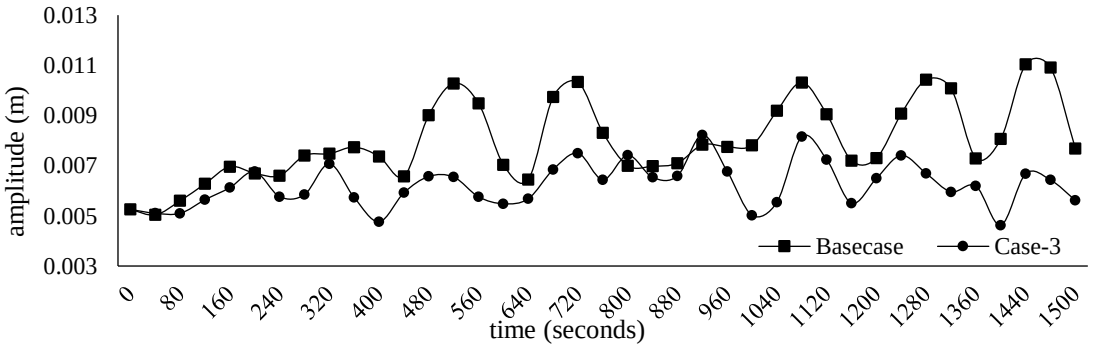

Figure 14. The amplitude of the dominant frequencies with time for basecase and case-3.

The interface deformations between 80 to 1480 seconds are plotted in Figure 15. The events of short-circuiting between the anode bottom and the interface are marked with the sign '▲'. The basecase interface (shown in left side of Figure 15) becomes highly unstable after perturbation of the (1, 0) mode, and frequent short-circuiting between the anode bottom and the interface can be observed, whereas interface is clearly more stable with fewer instances of short-circuiting for case-3 (shown in right side of Figure 15).

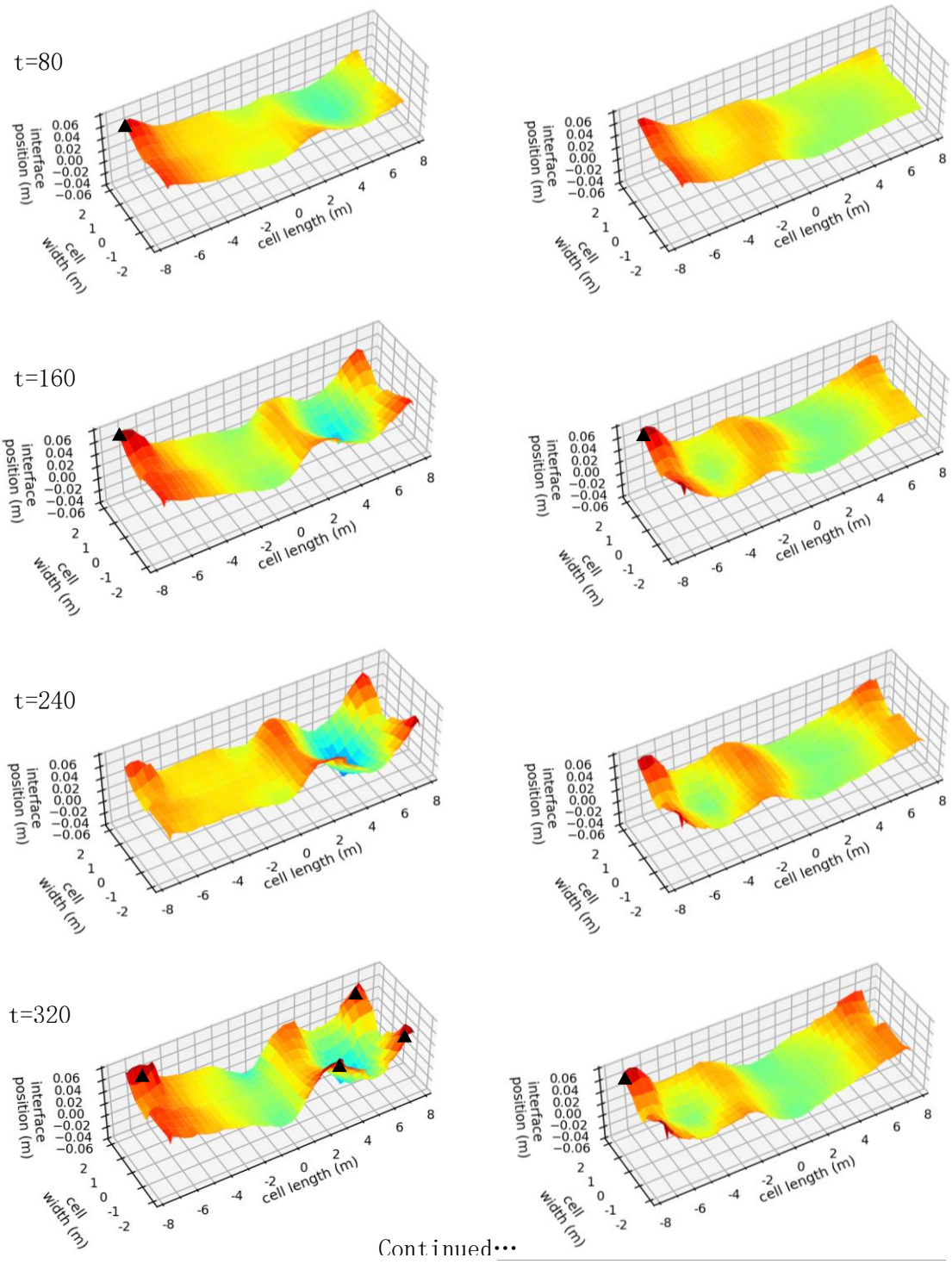
t=80
t=160
t=240
t=320
interface position (m)
cell width (m)
cell length (m)

Continued…

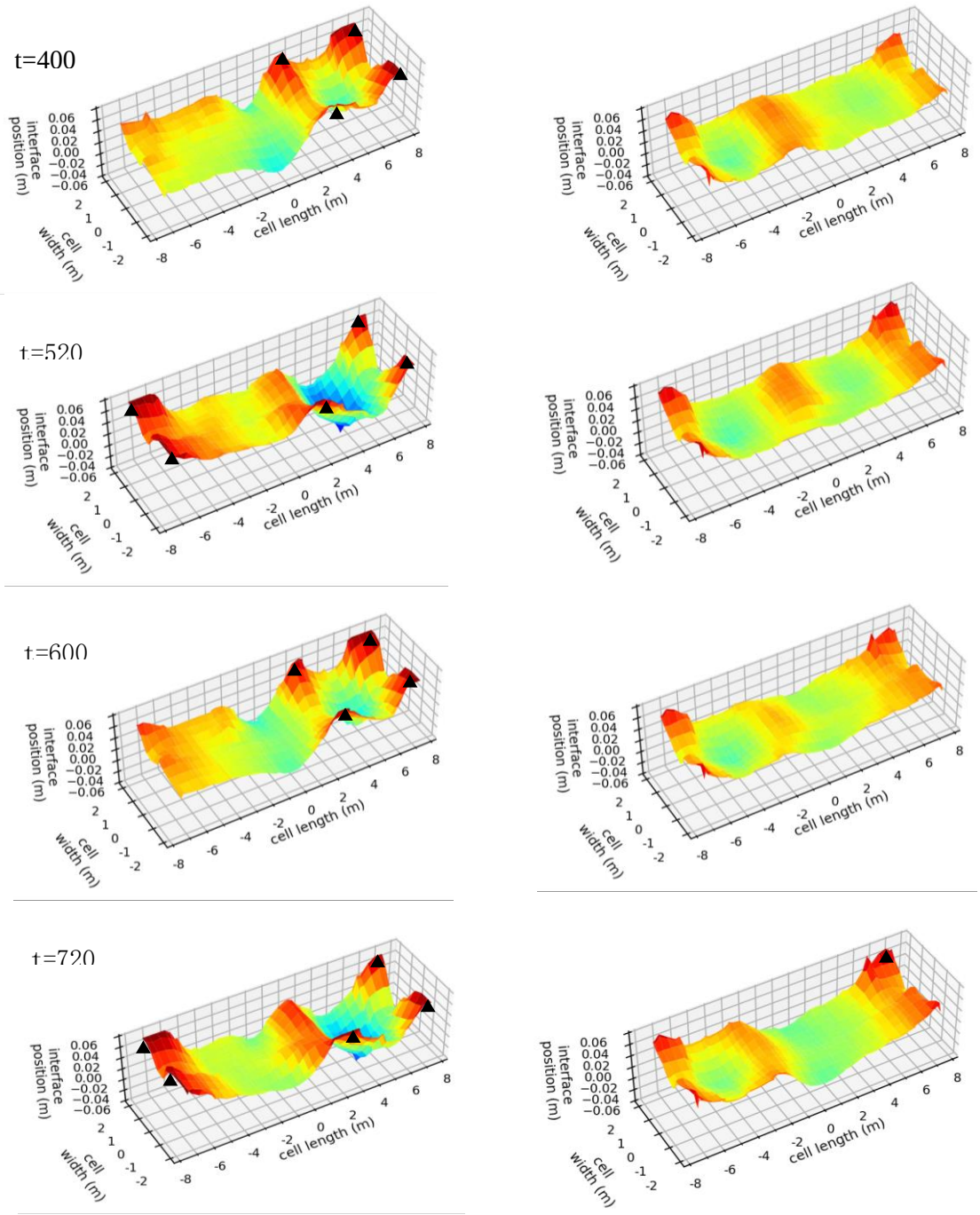
t=400
t=520
t=600
t=720
interface position (m)
cell width (m)
cell length (m)

Continued…

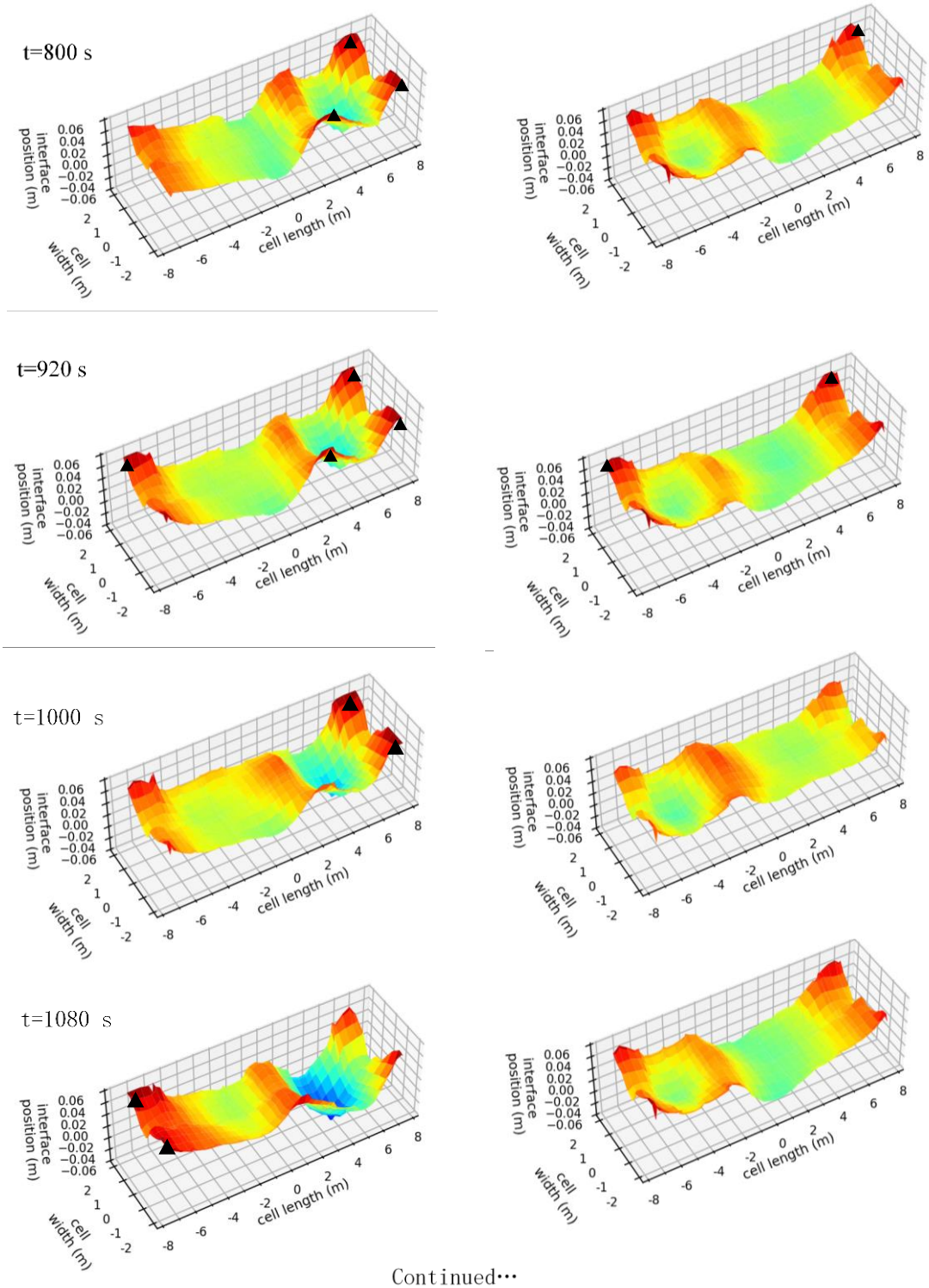
t=800 s
t=920 s
t=1000 s
t=1080 s
interface position (m)
cell width (m)
cell length (m)

Continued…

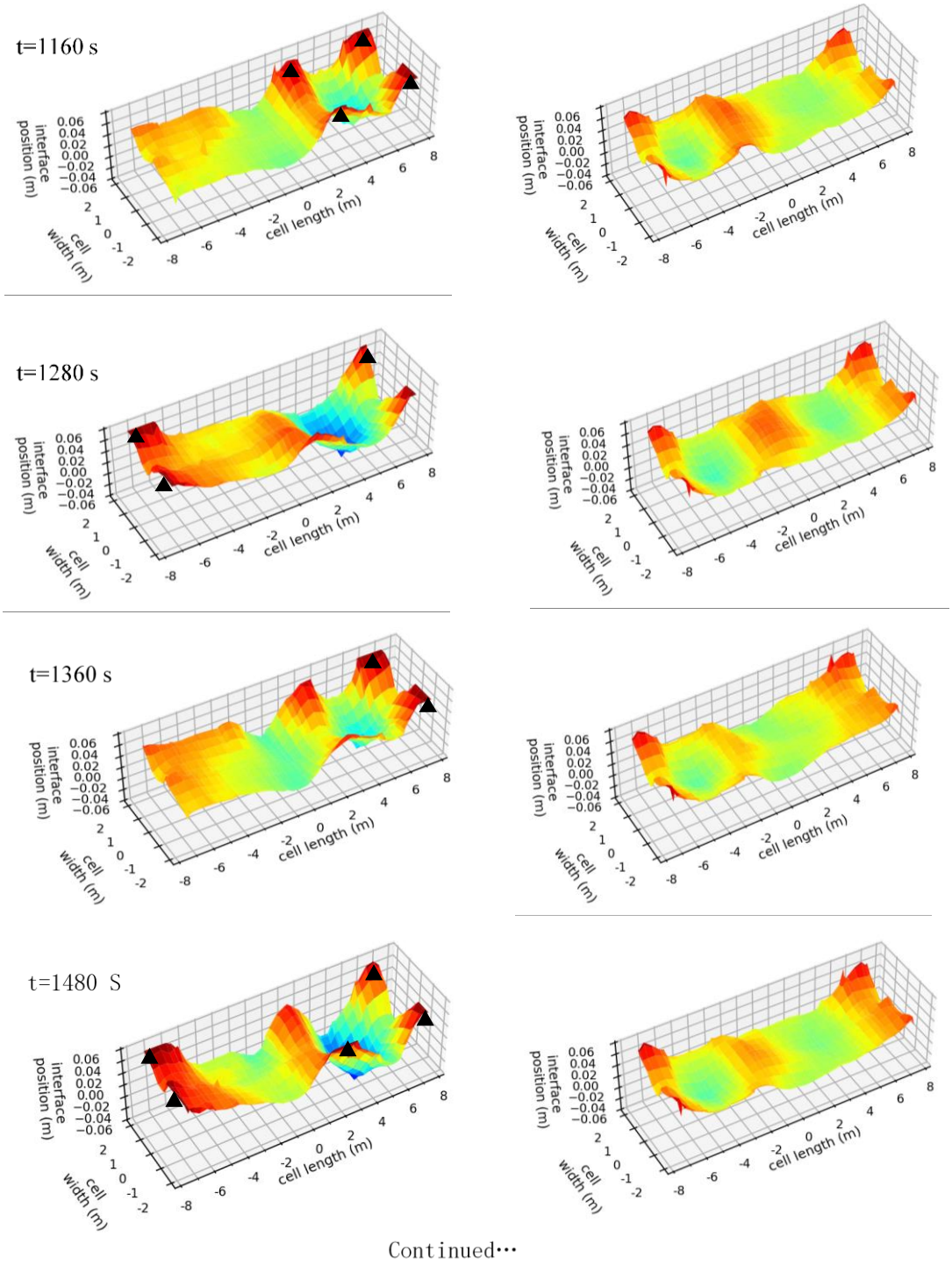

Figure 15. Interface deformation for basecase (left) and Case – 3 (right).

10. Conclusions

An antisymmetric distribution of the B_z helps to break the larger wavelength into smaller wavelength, which results in faster decay of the waves at aluminium-bath interface inside the reduction cells. The magnetic compensation loop in a potline helps to get the desired B_z distribution. Thus, the stability of the interface was studied after incorporating the effects of

magnetic compensation along the duct-side only, the tap-side only, and the both sides of a potline. The 3D MHD model based on the ESTER/PHOENICS software was used to analyze and compare the interface behavior under perturbed condition. The results of the transient simulation matches closely with the analytical solution of the internal gravity waves. The interfacial oscillation reduces significantly after magnetic compensation, and the amplitude of the waves was the smallest in presence of the compensation loop along the both sides of the potline. Therefore, a magnetic compensation loop installed along duct side as well as tap side of the potline can be a practical solution to counter the effects of neighboring potroom(s) or busbars at increased amperage.

11. References

1. Alton Tabereaux, Super-high amperage prebake cell technologies in operation at worldwide aluminum smelters, *Light Metal Age* 2017, 30-32.
2. Warren Haupin, Interpreting the components of cell voltage, *Light Metals* 1998, 531-537.
3. Nobuo Urata, K. Mori and H. Ikeuchi, Behavior of bath and molten metal in aluminum electrolytic cell, *Light Metals Japan* 1976, vol. 26, no. 11, 573.
4. Nobuo Urata, Magnetics & metal pad instability, *Light Metals* 1985, 330-335.
5. Thorleif Sele, Instabilities of the metal surface in electrolytic alumina reduction cells, *Metallurgical Transactions B* 1977, vol. 8B, 613-618.
6. Vinko Potocnik, Modelling of metal-bath interface waves in Hall-Heroult cells using ESTER/PHOENICS, *Light Metals* 1989, 227-235.
7. Nobuo Urata, Wave mode coupling and instability in the internal wave in aluminium reduction cells, *Light Metals* 2005, 455-460.
8. Vinko Potocnik, A-275 MHD Design, *Light Metals* 1986, 203-208.
9. A. D. Sneyd, Stability of fluid layers carrying a normal electric current, *J. Fluid Mech.* 1985, vol. 156, 223-236.
10. Peter A. Davidson and R. I. Lindsay, Stability of interfacial waves in aluminium reduction cells, *J. Fluid Mech.* 1998, vol. 362, 273-295.
11. Vinko Potocnik, Principles of MHD Design of aluminium electrolysis cells, *Light Metals* 1992, 1187-1193.
12. Vinko Potocnik and John Ludwig, New ESTER/PHOENICS – An upgraded 3D MHD modelling software for aluminium reduction cells, *Proceedings of the 40th International ICSOBA Conference*, Athens, Greece, 10-14 October 2022, Paper AL17, *Travaux* 51, 1199-1213.
13. K. Mori, K. Shiota, N. Urata and H. Ikeuchi, The Surface Oscillation of Liquid Metal in Aluminum Reduction Cells, *Light Metals* 1976, 77-96.